PHYSICAL REVIEW B **107**, 035140 (2023)

Exceptional heavy-fermion semimetals in three dimensions

Yu-Liang Tao,[1] Tao Qin ,[2,*] and Yong Xu [1,3,†]
[1]Center for Quantum Information, IIIS, Tsinghua University, Beijing 100084, People's Republic of China
[2]Department of Physics, School of Physics and Optoelectronics Engineering, Anhui University, Hefei, Anhui Province 230601, People's Republic of China
[3]Shanghai Qi Zhi Institute, Shanghai 200232, People's Republic of China

(Received 14 November 2021; revised 13 December 2021; accepted 10 January 2023; published 23 January 2023)

Topological heavy-fermion systems in three dimensions are usually classified as topological insulators or semimetals. Here, we theoretically predict a different type of heavy-fermion system (dubbed exceptional heavy-fermion semimetal) by studying a three-dimensional periodic Anderson model consisting of strongly correlated localized f electrons and itinerant conduction c electrons in a zinc-blende lattice. Due to the breaking of inversion symmetry, the quasiparticle lifetimes at different sublattices are distinct, leading to the emergence of Weyl exceptional rings in the complex pole of the Green's function at finite temperatures; such rings lead to the appearance of bounded Fermi surfaces (bulk Fermi disks). As temperatures rise, two pairs of Weyl exceptional rings merge into two exceptional rings with one bounded bulk Fermi surface (bulk Fermi tube), which are experimentally measurable by angle-resolved photoemission spectroscopy. Finally, we use the dynamical mean-field theory to calculate the spectral functions which illustrate the emergence of bulk Fermi tubes. Our work thus opens the door for studying exceptional heavy-fermion semimetal phases in three dimensions.

DOI: 10.1103/PhysRevB.107.035140

I. INTRODUCTION

Strongly correlated systems host a variety of intriguing phenomena beyond noninteracting electrons [1–5]. For instance, strongly correlated systems may allow for the existence of a bulk Fermi arc with ending points, which has been experimentally observed in the pseudogap phase of two-dimensional (2D) copper oxide high-temperature superconductors [6]. Such a bulk Fermi surface with boundaries is not allowed in a Hermitian noninteracting system with translational symmetry. Even in type-II Weyl semimetals, while a bulk Fermi surface can become open, boundaries are not allowed [7,8]. In this context, it has been theoretically shown that bulk Fermi arcs can also appear in 2D heavy-fermion systems due to the presence of exceptional points [9–14], where the single-particle effective Hamiltonian becomes nondiagonalizable. However, it is not clear whether bulk Fermi surfaces with boundaries can also emerge in a realistic three-dimensional (3D) strongly correlated material. The question is motivated by the recent discovery of exceptional rings with bounded Fermi surfaces in noninteracting non-Hermitian ultracold atomic systems or optical systems [15–23].

In heavy-fermion materials, apart from topological Kondo insulating phases [24–26], Weyl semimetal phases may also emerge, such as in noncentrosymmetric $\mathrm{CeRu_4Sn_6}$ or $\mathrm{Ce_3Bi_4Pd_3}$ [27–35]. In the paper, we study a microscopic periodic Anderson model describing an f-electron system, such as $\mathrm{CeRu_4Sn_6}$ or $\mathrm{Ce_3Bi_4Pd_3}$, and theoretically predict a different type of heavy-fermion state: exceptional heavy-fermion semimetals which have exceptional rings with bounded Fermi surfaces in the complex pole of the Green's function at finite temperatures. The model consists of strongly correlated localized f electrons and itinerant conduction electrons in a zinc-blende structure with A and B sublattices [see Fig. 1(a)]. The interactions for f electrons renormalize the effective one-body Hamiltonian through a self-energy in the retarded Green's function. In the presence of hybridization between f electrons and conduction electrons, the interactions not only renormalize parameters for a Weyl Hamiltonian but also transform Weyl points into exceptional rings. Such a ring arises from the fact that f electrons on A and B sublattices exhibit different lifetimes due to the broken inversion symmetry. Based on the second-order perturbation theory, we show that a Weyl point develops into a Weyl exceptional ring with a bulk Fermi disk as temperatures rise [see Fig. 1(d)]. As we further raise temperatures, two pairs of such Weyl exceptional rings merge into two exceptional rings [see Fig. 1(d)], leading to the emergence of a bounded Fermi surface in the shape of a tube. Finally, we utilize the dynamical mean-field theory (DMFT) to numerically compute the spectral functions illustrating the emergence of the bulk Fermi tubes in our system. Given the fact that a noncentrosymmetric heavy-fermion semimetal $\mathrm{Ce_3Bi_4Pd_3}$ has been experimentally identified [30,31], we expect that the Fermi tubes may be experimentally observed in the material.

II. PERIODIC ANDERSON MODELS

We start by considering a 3D periodic Anderson model consisting of strongly correlated localized f electrons and

---

[*] taoqin@ahu.edu.cn

[†] yongxuphy@tsinghua.edu.cn

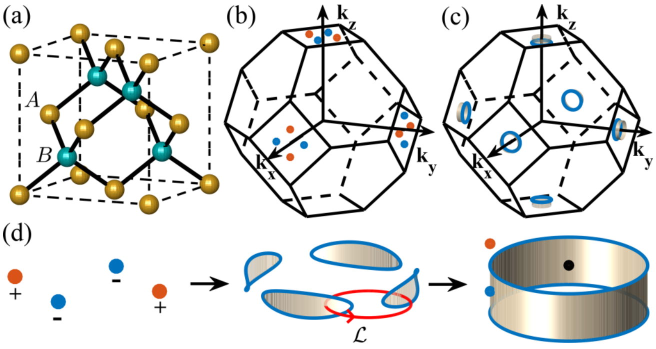

FIG. 1. (a) Schematic of the zinc-blende structure consisting of A and B sublattices. The first Brillouin zone of the fcc structure (b) with six pairs of Weyl points marked out as red (chiral charge $+1$) and blue (chiral charge -1) solid circles, which develop into three bulk Fermi tubes as shown in (c). (d) Schematic of the evolution of the zero-energy structure from four Weyl points to four Weyl exceptional rings marked by blue curves with bulk Fermi disks highlighted by the gold color; the Weyl exceptional rings finally develop into two exceptional rings with bulk Fermi tubes highlighted by the gold color. The winding number over the closed red circle enclosing two Weyl exceptional rings vanishes so that the two rings can merge.

conduction c electrons in a zinc-blende lattice with two sublattices denoted by A and B. The Hamiltonian reads

$$\hat{H} = \hat{H}_c + \hat{H}_f + \hat{H}_{cf}, \tag{1}$$

where $\hat{H}_c$, $\hat{H}_f$, and $\hat{H}_{cf}$ describe the conduction c electrons, localized f electrons, and their hybridization, respectively. Specifically, $\hat{H}_f = \varepsilon_f \sum_{j,\sigma} \hat{f}^\dagger_{j\sigma}\hat{f}_{j\sigma} + U\sum_j \hat{n}^f_{j\uparrow}\hat{n}^f_{j\downarrow}$ with ε_f being the energy of localized f electrons and U characterizing the Coulomb repulsion strength for f electrons, and $\hat{H}_{cf} = V\sum_{j,\sigma}(\hat{f}^\dagger_{j\sigma}\hat{c}_{j\sigma} + \text{H.c.})$ with V denoting the hybridization strength. Here, $\hat{c}_{j\sigma}$ and $\hat{f}_{j\sigma}$ ($\hat{c}^\dagger_{j\sigma}$ and $\hat{f}^\dagger_{j\sigma}$) are the fermion annihilation (creation) operators for a conduction and f electron with spin σ at site j, respectively; $\hat{n}^f_{j\sigma}$ refers to the number of f electrons with spin σ at site j. For conduction electrons, we write down its Hamiltonian in momentum space as $\hat{H}_c = \sum_{\boldsymbol{k}} \hat{\Psi}^\dagger_{\boldsymbol{k}} H_c(\boldsymbol{k})\hat{\Psi}_{\boldsymbol{k}}$, where $\hat{\Psi}^\dagger_{\boldsymbol{k}} = (\hat{c}^\dagger_{\boldsymbol{k}\uparrow,A} \quad \hat{c}^\dagger_{\boldsymbol{k}\uparrow,B} \quad \hat{c}^\dagger_{\boldsymbol{k}\downarrow,A} \quad \hat{c}^\dagger_{\boldsymbol{k}\downarrow,B})$ and

$$H_c(\boldsymbol{k}) = \sigma_0[u_1(\boldsymbol{k})\tau_x + u_2(\boldsymbol{k})\tau_y + m\tau_z] + \lambda\boldsymbol{D}\cdot\boldsymbol{\sigma}\tau_z, \tag{2}$$

which is a modified Fu-Kane-Mele model [36]. Here, σ_ν and τ_ν ($\nu = x, y, z$) represent Pauli matrices acting on spin and sublattice degrees of freedom, respectively, and σ_0 is the identity matrix. $u_1(\boldsymbol{k})$ and $u_2(\boldsymbol{k})$ are determined by the nearest-neighbor hopping between different sublattices with strength t, and $2m$ represents the amount of the on-site potential difference on sublattices A and B, which breaks inversion symmetry. $D_\nu(\boldsymbol{k})$ ($\nu = x, y, z$) is determined by the spin-orbit coupling with strength λ. The specific expressions of u_1, u_2, and D_ν can be found in Appendix A. To simplify notations, we have set the lattice constant $a = 1$.

Without interactions, when $|m| < 4|\lambda|$, the Hamiltonian of conduction electrons exhibits six pairs of Weyl points located at $(\pm k_0, 0, 2\pi)$, $(2\pi, 0, \pm k_0)$, $(0, \pm k_0, 2\pi)$, $(0, 2\pi, \pm k_0)$, $(\pm k_0, 2\pi, 0)$, and $(2\pi, \pm k_0, 0)$, where $k_0 = 2\sin^{-1}(|m/4\lambda|)$ with $0 < k_0 < \pi$ [see the locations of Weyl points in the first Brillouin zone in Fig. 1(b) and the band structure in Fig. 2(b)]. These points annihilate each other through the critical point $|m| = 4|\lambda|$, leading to a topologically trivial insulator when $|m| > 4|\lambda|$.

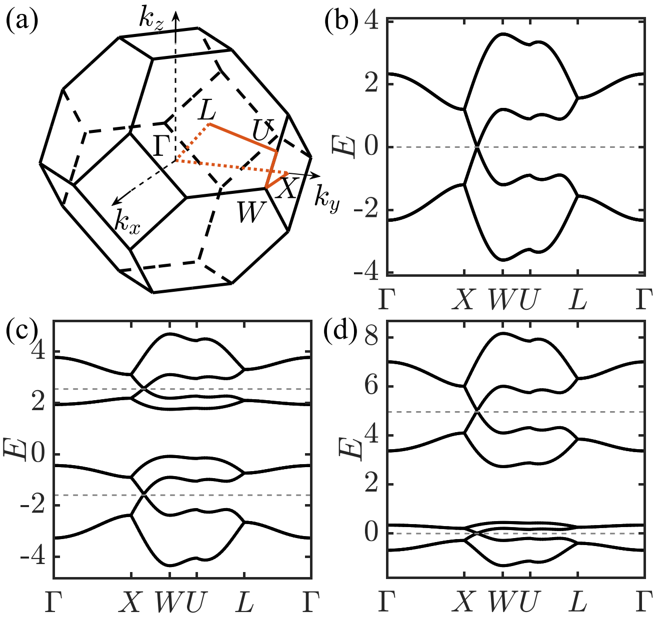

FIG. 2. (a) The first Brillouin zone of the fcc structure. The red lines denote the high symmetry path. (b) The band structure of the Hamiltonian $H_c(\boldsymbol{k})$ of conduction c electrons along the high symmetry path. The band structure of the whole Hamiltonian $H_0(\boldsymbol{k})$ along the high symmetry path (c) without ε_s, and (d) with ε_s. Here, $t = 0.5$, $m = 1.2$, $\lambda = 0.6$, $V = 2$, $\varepsilon_f = 1$, and $\varepsilon_s = 4$.

In the presence of localized f electrons and the hybridization between f and c electrons, the Hamiltonian in momentum space without interactions is expressed as

$$H_0(\boldsymbol{k}) = \begin{pmatrix} \varepsilon_f & V \\ V & H_c(\boldsymbol{k}) \end{pmatrix}. \tag{3}$$

The hybridization changes the energy $\varepsilon_{c,i}(\boldsymbol{k})$ ($i = 1, 2, 3, 4$) of $H_c(\boldsymbol{k})$ to two energies $\varepsilon_{i,\pm}(\boldsymbol{k}) = \{[\varepsilon_f + \varepsilon_{c,i}(\boldsymbol{k})] \pm \sqrt{[\varepsilon_f - \varepsilon_{c,i}(\boldsymbol{k})]^2 + 4V^2}\}/2$. Thus, a Weyl point at zero energy in $H_c(\boldsymbol{k})$ becomes two Weyl points with different energies: One has a negative energy corresponding to a quarter filling [see Fig. 2(c)]. For convenience, we will add a constant energy shift $\varepsilon_s = V^2/\varepsilon_f$ in H_c so that the energy at Weyl points between the second and third bands is fixed at the zero energy [see Fig. 2(d)]. Note that such a shift will not change the physics.

In the presence of interactions, we consider the retarded Green's function at the energy ω

$$G^R(\omega, \boldsymbol{k}) = [\omega + \mu - H_0(\boldsymbol{k}) - \Sigma(\omega, \boldsymbol{k})]^{-1}, \tag{4}$$

where μ is the chemical potential and $\Sigma(\omega, \boldsymbol{k})$ is the self-energy. Similar to the two-dimensional case [9], since there are interactions only for f electrons, only f electrons acquire a nonzero self-energy,

$$\Sigma(\omega) = \begin{pmatrix} \Sigma^f(\omega) & 0 \\ 0 & 0 \end{pmatrix}. \tag{5}$$

Here, we also assume that the self-energy is independent of quasimomenta because we consider heavy f electrons without dispersion (in other words, the temperature is high compared to the bandwidth of f electrons) [9]. With time-reversal symmetry, Σ^f is independent of spins, i.e., $[\Sigma^f]_{\sigma\sigma'} = [\Sigma^f]_{\sigma\sigma'}\delta_{\sigma\sigma'}$. However, without inversion symmetry, Σ^f can have different components at different sublattices. At finite temperatures, the self-energy takes complex values due to quasiparticle finite lifetimes. The breaking of inversion symmetry thus leads to different lifetimes for electrons at different sublattices, resulting in the appearance of Weyl exceptional rings as shown in the following discussion.

To demonstrate that exceptional rings emerge in the presence of lifetime difference of electrons at different sublattices, we expand the self-energy in the Taylor series up to the first order with respect to ω,

$$\Sigma^f(\omega) \approx a_0 - i\Gamma_0 + (a_1 - i\Gamma_1)\tau_z + a_{0\omega}\omega + a_{1\omega}\omega\tau_z, \tag{6}$$

where $a_0 + a_1$ and $a_0 - a_1$ ($a_{0\omega} + a_{1\omega}$ and $a_{0\omega} - a_{1\omega}$) describe the zeroth-order (first-order) real parts of the self-energy at sublattices A and B, respectively, and $\Gamma_0 + \Gamma_1$ and $\Gamma_0 - \Gamma_1$ depict the inverse of quasiparticle lifetimes at sublattices A and B, respectively. To present clearly, we here do not consider the imaginary contribution in the first-order correction (see Appendix B for the derivation). In this case, the first-order terms only renormalize parameters as $\varepsilon_{fr} = \varepsilon_f + a_0 \rightarrow \bar{\varepsilon}_{fr} = [(Z_A + Z_B)\varepsilon_{fr} + (Z_A - Z_B)a_1]/2$, $\Gamma_0 \rightarrow \bar{\Gamma}_0 = [(Z_A + Z_B)\Gamma_0 + (Z_A - Z_B)\Gamma_1]/2$, $a_1 \rightarrow \bar{a}_1 = [(Z_A - Z_B)\varepsilon_{fr} + (Z_A + Z_B)a_1]/2$, $\Gamma_1 \rightarrow \bar{\Gamma}_1 = [(Z_A - Z_B)\Gamma_0 + (Z_A + Z_B)\Gamma_1]/2$ with $Z_A = 1/(1 - a_{0\omega} - a_{1\omega})$, and $Z_B = 1/(1 - a_{0\omega} + a_{1\omega})$. The first-order terms also renormalize the coupling matrix $\mathrm{diag}(V, V)$ to $\mathrm{diag}(V_A, V_B)$ with $V_A = \sqrt{Z_A}V$ and $V_B = \sqrt{Z_B}V$. When $\Gamma_0 = \Gamma_1 = 0$, we add an energy shift $\varepsilon_s = (\bar{\varepsilon}_{fr}\bar{V}^2 + V_0\bar{a}_1)/(\bar{\varepsilon}_{fr}^2 - \bar{a}_1^2)$ with $\bar{V} = \sqrt{V_1^2 + V_2^2}$, $V_0 = -2V_1V_2$, $V_1 = (V_A + V_B)/2$, and $V_2 = (V_A - V_B)/2$ in H_c to fix the energy of Weyl points at zero corresponding to a quarter filling. There, the locations of Weyl points in momentum space are still determined by H_c with a renormalized mass $\bar{m} = m - d_{z0}$ with $d_{z0} = (\bar{V}^2 a_1 + V_0\bar{\varepsilon}_{fr})/(a_1^2 - \bar{\varepsilon}_{fr}^2)$. In fact, only k_0 is changed to $\bar{k}_0 = 2\sin^{-1}(|\bar{m}/4\lambda|)$ with $0 < \bar{k}_0 < \pi$.

We now study the effects of the imaginary parts of the self-energy on the pole of the Green's function. To derive an analytical expression of the energy close to a Weyl point, we assume that Γ_0, Γ_1, a_1, $a_{0\omega}$, and $a_{1\omega}$ are small quantities. Slightly away from a Weyl point $\boldsymbol{k}_W$ determined by $u_1(\boldsymbol{k}_W) = u_2(\boldsymbol{k}_W) = 0$ and $\bar{m} + \alpha\lambda D(\boldsymbol{k}_W) = 0$ with $D = \sqrt{D_x^2 + D_y^2 + D_z^2}$ and $\alpha = \pm 1$, u_1, u_2, and $\bar{m} + \alpha\lambda D(\boldsymbol{k}_W)$ are small quantities. Specifically, $u_1(\boldsymbol{k}_W + \delta\boldsymbol{k}) = d_x$, $u_2(\boldsymbol{k}_W + \delta\boldsymbol{k}) = d_y$, and $\bar{m} + \alpha\lambda D(\boldsymbol{k}_W + \delta\boldsymbol{k}) = d_z$, where $\delta\boldsymbol{k}$ is a small vector measured with respect to $\boldsymbol{k}_W$. The energy is derived as

$$\omega = -i\bar{\Gamma}_0\bar{v}_0 \pm \sqrt{\bar{v}_1^2\left[d_x^2 + d_y^2 + (d_z - i\bar{\gamma}_0)^2\right]}, \tag{7}$$

where $\bar{v}_0 = \varepsilon_s/(\bar{\varepsilon}_{fr} + \varepsilon_s)$, $\bar{v}_1 = \bar{\varepsilon}_{fr}/(\bar{\varepsilon}_{fr} + \varepsilon_s)$, and $\bar{\gamma}_0 = \varepsilon_s\bar{\Gamma}_1/\bar{\varepsilon}_{fr}$. Remarkably, the inverse lifetime difference Γ_1 at two sublattices leads to the emergence of a Weyl exceptional ring determined by $d_z = 0$ and $d_x^2 + d_y^2 = \gamma_0^2$, where the Hamiltonian becomes nondiagonalizable. One of the authors has established that a Weyl exceptional ring is characterized by two topological invariants: the Chern number and the Berry phase [15]. In addition, the real part of the energy vanishes inside the ring, leading to a bulk Fermi surface in the shape of a Fermi disk. Specifically, consider the two pairs of Weyl points on the $k_z = 2\pi$ plane. Based on the perturbation theory up to the second order (see Appendix C for details), as temperatures rise, the difference of the inverse of quasiparticle lifetimes Γ_1 gets bigger, leading to the development of four Weyl exceptional rings from four Weyl points; as Γ_1 further increases, the neighboring Weyl exceptional rings merge and become two exceptional rings [see Fig. 1(d)]. The two rings serve as two boundaries of a bounded Fermi surface in the shape of a Fermi tube [there is a total of three Fermi tubes in the first Brillouin zone as shown in Fig. 1(c)]. The mergence can happen due to the fact that the winding number defined as [37–39]

$$W_{\mathcal{L}} = \frac{1}{2\pi}\oint_{\mathcal{L}} d\boldsymbol{k} \cdot \nabla_{\boldsymbol{k}}[\arg(\omega_+) + \arg(\omega_-)], \tag{8}$$

vanishes over a closed path enclosing two neighboring rings [see Fig. 1(d)]. Here, ω_- and ω_+ refer to the two energies close to zero energy which are numerically obtained by approximating the self-energy up to the first order.

The bounded Fermi surface manifests in the spectral functions, which can be experimentally measured by angle-resolved photoemission spectroscopy (ARPES). The spectral functions read

$$\rho(\omega, \mathbf{k}) = -(1/\pi)\mathrm{Im}\mathrm{Tr}[G^R(\omega, \mathbf{k})], \tag{9}$$

which reflects the pole information of the Green's function. To demonstrate, we calculate the self-energy by the perturbation theory up to the second order (see Appendix C) and then evaluate the spectral functions (see Fig. 3). Specifically, when $T = 1/20$, there are two pairs of Weyl exceptional rings with four bulk Fermi disks [see Fig. 1(d) (center) and Fig. 4(a)]. Note that in Figs. 3–6, we take k_B Kelvin and Kelvin as energy and temperature units, respectively. We illustrate the Fermi disk structures by the sectional view of the zero-energy spectral function in the $k_y = 0$ plane around $k_z = 2\pi$ and in the $k_z = 2\pi$ plane. The former shows two short bright lines and the latter shows four bright arcs. The arcs are connected to form a ring with much smaller values in the connecting parts, which arises from the fact that the existence of Γ_0 widens the spectral functions. When the temperature is raised to $T = 1/6$, two pairs of Weyl exceptional rings become two rings with a bulk Fermi tube [Fig. 4(b)]. Similarly, the sectional view of the zero-energy spectral function reflects the bulk Fermi tube structure: There are two bright lines in the $k_y = 0$ plane and a bright circle in the $k_z = 2\pi$ plane. Figure 5(a) further displays the spectral functions with respect to the energy for three typical points in momentum space. On the Fermi tube, the spectral function exhibits a peak at zero energy; away from the tube, it develops a minimum around the zero energy and peaks away from the zero energy, consistent with the energy spectrum structure (see Appendix D for details).

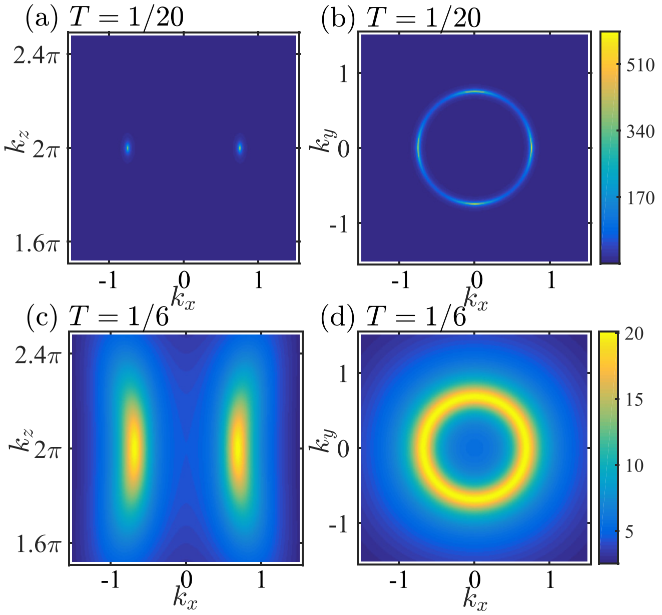

FIG. 3. The sectional view of the zero-energy spectral functions (a), (c) in the $k_y = 0$ plane around $k_z = 2\pi$ and (b), (d) in the $k_z = 2\pi$ plane, which are calculated by the perturbation theory. The results imply the existence of bulk Fermi disks in (a) and (b) or bulk Fermi tubes in (c) and (d) due to the appearance of Weyl exceptional rings [see Fig. 4(a)] at the temperature $T = 1/20$ or a pair of exceptional rings [see Fig. 4(b)] at $T = 1/6$, respectively. Here, $t = 0.5$, $m = 1.2$, $\lambda = 0.6$, $V = 2$, $U = 2$, $\varepsilon_f = 1$, and $\varepsilon_s = 4$.

III. SPECTRAL FUNCTIONS CALCULATED BY THE DMFT

In order to analyze the interacting effects more accurately, we adopt the DMFT with the segment-based hybridization-expansion continuous-time quantum Monte Carlo impurity solver (CT-HYB) implemented in the toolkit Triqs [40]. Within the DMFT, we treat the self-energy $\Sigma(\boldsymbol{k}, \omega)$ in Eq. (4) approximately as $\Sigma(\omega)$ based on the local fluctuation approximation. We also numerically confirm that the off-diagonal entries in $\Sigma^f(\omega)$ are much smaller than the diagonal ones. Even though the self-energy is $\boldsymbol{k}$ independent, it is beyond the reach of the perturbation theory for intermediate and strong interactions.

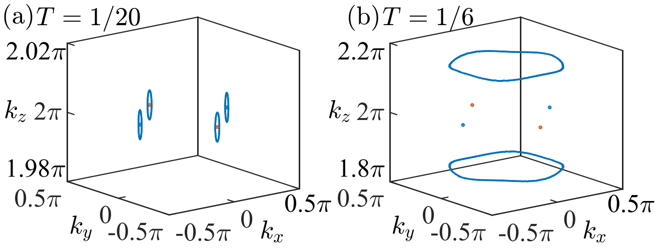

FIG. 4. The contours of exceptional rings around $k_z = 2\pi$ at the temperature (a) $T = 1/20$ and (b) $T = 1/6$, which are calculated by the perturbation theory with an approximation, $a_{0\omega} \approx 0$ and $a_{1\omega} \approx 0$. Blue/red nodes denote the original Weyl points. Here, $t = 0.5$, $m = 1.2$, $\lambda = 0.6$, $V = 2$, $U = 2$, $\varepsilon_f = 1$, and $\varepsilon_s = 4$.

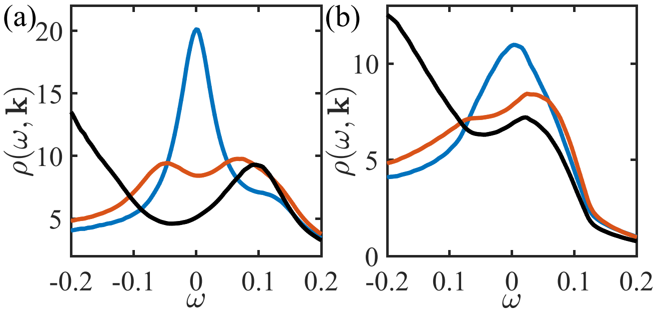

FIG. 5. The spectral function versus the energy for three typical points in momentum space. The positions of these points are schematically marked out by the corresponding colored solid circles in Fig. 1(d) (right). (a) is calculated by the perturbation theory with the same system parameters as in Fig. 3 at $T = 1/6$, and (b) is calculated by the DMFT at $T = 1/11$ with $t = 0.5$, $m = 1.2$, $\lambda = 0.6$, $V = 2$, $U = 2.5$, $\varepsilon_f = 0.275$, and $\varepsilon_s = 4$.

To calculate the spectral function $\rho(\omega, \boldsymbol{k})$, we first employ the DMFT to compute the imaginary time Green's function and then carry out the numerical analytic continuation of the imaginary time self-energy $\Sigma(i\omega_n)$ with Triqs/maxent. For the numerical analytic continuation, we find that the output of $\Sigma(\omega)$ is extremely sensitive to the noise in $\Sigma(i\omega_n)$. To ensure the reliability of our results, we need to reduce the amplitude of noises as far as possible. In practice, we utilize the Legendre polynomial to reduce high-frequency noises during self-consistent iterations and average multistep iterative results of $\Sigma(i\omega_n)$ as the final output after convergence.

Figure 6 demonstrates the sectional view of the zero-energy spectral functions around $k_z = 2\pi$ at $T = 1/11$ obtained by the DMFT calculation. We see clearly the existence of bulk Fermi tubes, which is consistent with the results computed by the perturbation theory. The spectral functions with respect to the energy exhibit a peak at zero energy in a momentum on a Fermi tube and peaks away from zero energy in momenta away from the Fermi tube [see Fig. 5(b)]. The results are qualitatively consistent with those obtained by the perturbation theory. However, compared with the results from the perturbation theory calculations, the contrast between the values of the peak and background of $\rho(\omega, \boldsymbol{k})$ from the DMFT

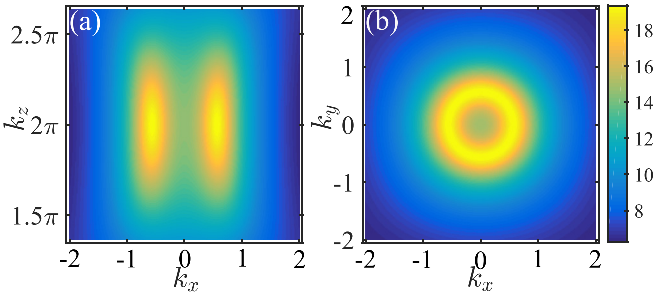

FIG. 6. The sectional view of the zero-energy spectral functions (a) in the $k_y = 0$ plane around $k_z = 2\pi$ and (b) in the $k_z = 2\pi$ plane, which are calculated by the DMFT at $T = 1/11$. The results indicate the existence of bulk Fermi tubes due to the appearance of a pair of exceptional rings. Here, $t = 0.5$, $m = 1.2$, $\lambda = 0.6$, $V = 2$, $U = 2.5$, $\varepsilon_f = 0.275$, and $\varepsilon_s = 4$.

calculations is lower. We attribute this to a smaller value of Γ_1/Γ_0 from the DMFT than that from the perturbation theory, generating a relatively larger background. Because the DMFT is a better way to treat interactions, one can attribute the features above to interaction effects. Clearly, the DMFT reveals that the bulk Fermi tubes benefit from the complex-valued self-energy from intermediate interactions. However, one can expect that this interesting phenomenon would be finally suppressed by strong interactions when the system enters into the Mott insulator phase (see Appendix E for details).

IV. CONCLUSION

In summary, we have found a different type of 3D heavy-fermion phase: exceptional heavy-fermion semimetals which possess exceptional rings in the complex pole of the Green's function at finite temperatures. Such rings give rise to bounded bulk Fermi surfaces such as Fermi disks or Fermi tubes manifesting in the spectral functions, which are experimentally measurable by ARPES. We finally use the dynamical mean-field theory to calculate the spectral functions in our system, revealing the emergence of bulk Fermi tubes. Recently, a noncentrosymmetric heavy-fermion semimetal $\mathrm{Ce_3Bi_4Pd_3}$ has been experimentally identified [30,31], and we may expect that bulk Fermi tubes may be experimentally observed in the material. Our work thus opens another direction for studying exceptional heavy-fermion semimetal phases in 3D.

ACKNOWLEDGMENTS

We thank Adriano Amaricci, Liang Du, Michel Ferrero, Li Huang, Kai Li, Yuki Nagai, Yilin Wang, Nils Wentzell, and Yan-Bin Yang for helpful discussions and communications. This work is supported by the National Natural Science Foundation of China (Grants No. 11974201 and No. U2032164), Tsinghua University Dushi Program and the Shanghai Qi Zhi Institute.

APPENDIX A: HOPPING TERMS IN THE HAMILTONIAN

The hopping terms u_1, u_2, and D_ν $(\nu = x, y, z)$ in the Hamiltonian (2) in the main text are given by

$$u_1(\boldsymbol{k}) = t\left[1 + \sum_{n=1}^{3} \cos(\boldsymbol{k}\cdot\boldsymbol{a}_n)\right], \tag{A1}$$

$$u_2(\boldsymbol{k}) = t\sum_{n=1}^{3} \sin(\boldsymbol{k}\cdot\boldsymbol{a}_n), \tag{A2}$$

$$\begin{aligned} D_x(\boldsymbol{k}) = \lambda\{&\sin(\boldsymbol{k}\cdot\boldsymbol{a}_2) - \sin(\boldsymbol{k}\cdot\boldsymbol{a}_3)\sin[\boldsymbol{k}\cdot(\boldsymbol{a}_2-\boldsymbol{a}_1)] \\ &+ \sin[\boldsymbol{k}\cdot(\boldsymbol{a}_3-\boldsymbol{a}_1)]\}, \end{aligned} \tag{A3}$$

$$\begin{aligned} D_y(\boldsymbol{k}) = \lambda\{&\sin(\boldsymbol{k}\cdot\boldsymbol{a}_3) - \sin(\boldsymbol{k}\cdot\boldsymbol{a}_1)\sin[\boldsymbol{k}\cdot(\boldsymbol{a}_3-\boldsymbol{a}_2)] \\ &+ \sin[\boldsymbol{k}\cdot(\boldsymbol{a}_1-\boldsymbol{a}_2)]\}, \end{aligned} \tag{A4}$$

$$\begin{aligned} D_z(\boldsymbol{k}) = \lambda\{&\sin(\boldsymbol{k}\cdot\boldsymbol{a}_1) - \sin(\boldsymbol{k}\cdot\boldsymbol{a}_2)\sin[\boldsymbol{k}\cdot(\boldsymbol{a}_1-\boldsymbol{a}_3)] \\ &+ \sin[\boldsymbol{k}\cdot(\boldsymbol{a}_2-\boldsymbol{a}_3)]\}, \end{aligned} \tag{A5}$$

where $\boldsymbol{a}_1 = (0, 1/2, 1/2)$, $\boldsymbol{a}_2 = (1/2, 0, 1/2)$, and $\boldsymbol{a}_3 = (1/2, 1/2, 0)$ are the lattice vectors for a fcc lattice.

APPENDIX B: THE ENERGY DISPERSION IN THE PRESENCE OF THE SELF-ENERGY

In this Appendix, we will derive the energy dispersion near a Weyl point in the presence of the self-energy. For clarity, we first study a simple case where the self-energy contains only the terms that are independent of the energy, and show the emergence of Weyl exceptional rings arising from the quasiparticle lifetime difference at different sublattices. After that, we demonstrate that the effects of including a term in the self-energy that is linearly dependent of the energy is the renormalization of system parameters, which does not affect the qualitative feature of the energy spectrum.

1. Energy spectra in the presence of the real energy-independent self-energy

We now study the effects of the terms in the self-energy that are independent of the energy, which read

$$\Sigma^f = a_0 - i\Gamma_0 + (a_1 - i\Gamma_1)\tau_z\sigma_0, \tag{B1}$$

where $a_0 + a_1$ and $a_0 - a_1$ denote the zeroth-order real parts of the self-energy at sublattices A and B, respectively, and $\Gamma_0 + \Gamma_1$ and $\Gamma_0 - \Gamma_1$ denote the inverse of quasiparticle lifetimes at sublattices A and B, respectively. In the derivation, we first consider the complex self-energy and then make Γ_0 and Γ_1 zero. The inverse of the Green's function is

$$G^{-1} = \omega - \begin{pmatrix} \tilde{\varepsilon}_f + a\tau_z & V \\ V & H_c + \varepsilon_s \end{pmatrix}, \tag{B2}$$

where $\tilde{\varepsilon}_f = \varepsilon_f + a_0 - i\Gamma_0 = \varepsilon_{fr} - i\Gamma_0$ and $a = a_1 - i\Gamma_1$. Here

$$H_c = \sigma_0(u_1\tau_x + u_2\tau_y + m\tau_z) + \lambda\boldsymbol{D}\cdot\boldsymbol{\sigma}\tau_z. \tag{B3}$$

We can transform this matrix into a block form

$$\tilde{H}_c = S^\dagger H_c S = \begin{pmatrix} h_+ & 0 \\ 0 & h_- \end{pmatrix} = \boldsymbol{u}\cdot\boldsymbol{\tau} + \lambda D\sigma_z\tau_z \tag{B4}$$

with $h_\pm = u_1\tau_x + u_2\tau_y + (m \pm D\lambda)\tau_z$, $u_x = u_1$, $u_y = u_2$, and $u_z = m$ by the matrix

$$S = (|u_+\rangle \quad |u_-\rangle)\tau_0. \tag{B5}$$

Here $|u_\pm\rangle$ are eigenstates of $\boldsymbol{D}\cdot\boldsymbol{\sigma}$ corresponding to eigenvalues $\pm D$, i.e., $\boldsymbol{D}\cdot\boldsymbol{\sigma}|u_\pm\rangle = \pm D|u_\pm\rangle$.

The determinant of the inverse of the Green's function can be simplified as

$$\begin{aligned} \det(G^{-1}) &= \begin{vmatrix} \tilde{\varepsilon}_f + a\tau_z - \omega & V \\ V & \tilde{H}_c + \varepsilon_s - \omega \end{vmatrix} \\ &= |(\tilde{\varepsilon}_f + a\tau_z - \omega)(H_c + \varepsilon_s - \omega) - V^2| \\ &= |S^\dagger[(\tilde{\varepsilon}_f + a\tau_z - \omega)(H_c + \varepsilon_s - \omega) - V^2]S| \\ &= |(\tilde{\varepsilon}_f + a\tau_z - \omega)(\tilde{H}_c + \varepsilon_s - \omega) - V^2| \\ &= |(\tilde{\varepsilon}_f + a\tau_z - \omega)(\boldsymbol{u}\cdot\boldsymbol{\tau} + \lambda D\sigma_z\tau_z + \varepsilon_s - \omega) - V^2| \\ &= \begin{vmatrix} b_{0+} + \boldsymbol{b}_+\cdot\boldsymbol{\tau} & 0 \\ 0 & b_{0-} + \boldsymbol{b}_-\cdot\boldsymbol{\tau} \end{vmatrix} \\ &= \left(b_{0+}^2 - b_+^2\right)\left(b_{0-}^2 - b_-^2\right), \end{aligned} \tag{B6}$$

where

$$
\begin{aligned}
b_{0\alpha} &= \omega^2 - V^2 - \omega(\tilde{\varepsilon}_f + \varepsilon_s) + \tilde{\varepsilon}_f\varepsilon_s + au'_z,\\
b_x &= (-\omega + \tilde{\varepsilon}_f)u_x - iau_y,\\
b_y &= (-\omega + \tilde{\varepsilon}_f)u_y + iau_x,\\
b_{z\alpha} &= -\omega(u_z + a + \alpha\lambda D) + \tilde{\varepsilon}_f u'_z + a\varepsilon_s,\\
b_\alpha &= \sqrt{b_x^2 + b_y^2 + b_{z\alpha}^2}
\end{aligned}
$$

with $u'_z = u_z + \alpha\lambda D$ and $\alpha = \pm 1$. In the derivation, we have used the identity

$$\det\begin{pmatrix} A & B \\ C & D \end{pmatrix} = \det(AD - ACA^{-1}B), \tag{B7}$$

where A, B, C, and D are $n\times n$, $n\times m$, $m\times n$, and $m\times m$ matrices, respectively, and A is invertible. It follows immediately from the identity

$$\begin{pmatrix} A & B \\ C & D \end{pmatrix}\begin{pmatrix} I & -A^{-1}B \\ 0 & I \end{pmatrix} = \begin{pmatrix} A & 0 \\ C & D - CA^{-1}B \end{pmatrix}. \tag{B8}$$

We also have

$$b_x^2 + b_y^2 = [(-\omega + \tilde{\varepsilon}_f)^2 - a^2]\big(u_x^2 + u_y^2\big). \tag{B9}$$

The poles of the Green's function are determined by $\det(G^{-1}) = 0$ which yields

$$b_{0\alpha}^2 = b_\alpha^2.$$

To determine the position of a Weyl point in momentum space, we suppose that $\tilde{\varepsilon}_f$ and a are real ($\tilde{\varepsilon}_f = \varepsilon_{fr}$ and $a = a_1$). The existence of a Weyl point at zero energy $\omega = 0$ requires that $b_0(\omega = 0) = b(\omega = 0)$ and $b_0(\omega = 0) = -b(\omega = 0)$ so that

$$b_0(\omega = 0) = 0, \tag{B10}$$

$$b(\omega = 0) = 0, \tag{B11}$$

where we have dropped the subscript α to simplify notations. Specifically, we require that

$$-V^2 + \tilde{\varepsilon}_f\varepsilon_s + au'_z = 0, \tag{B12}$$

$$u_x = u_y = 0, \tag{B13}$$

$$\tilde{\varepsilon}_f u'_z + a\varepsilon_s = 0. \tag{B14}$$

These equations indicate that the location of a Weyl point is the same as that in H_c with an effective mass $\tilde{m} = m - u'_z$. In fact, only k_0 changes to $\tilde{k}_0 = 2\sin^{-1}(|\tilde{m}/4\lambda|)$. These equations further lead to

$$u'_z = u_{Wz} = \frac{-a_1V^2}{\varepsilon_{fr}^2 - a_1^2}, \tag{B15}$$

$$\varepsilon_s = \frac{\varepsilon_{fr}V^2}{\varepsilon_{fr}^2 - a_1^2}. \tag{B16}$$

We are now interested in deriving the energy dispersion near a Weyl point. By expanding u_x, u_y, and u'_z around zero, that is, $u_x = d_x$, $u_y = d_y$, and $u'_z = u_{Wz} + d_z$ where d_x, d_y, and d_z are the first-order small quantities, we obtain

$$b_0 = \omega^2 - \omega(\varepsilon_{fr} + \varepsilon_s) + a_1d_z, \tag{B17}$$

$$b_x = (-\omega + \varepsilon_{fr})d_x - ia_1d_y, \tag{B18}$$

$$b_y = (-\omega + \varepsilon_{fr})d_y + ia_1d_x, \tag{B19}$$

$$b_z = -\omega(d_z + a_1 + u_{Wz}) + \varepsilon_{fr}d_z. \tag{B20}$$

Based on these expressions, we derive the energy spectrum around zero energy up to the first order as

$$\omega \approx \frac{2d_z\varepsilon_{fr}u_{Wz} \pm \sqrt{v_x^2\big(d_x^2 + d_y^2\big) + v_z^2d_z^2}}{c_0}, \tag{B21}$$

where $v_x^2 = (a_r^2 - \varepsilon_{fr}^2)c_0$, $v_z^2 = v_x^2 + 4\varepsilon_{fr}^2u_{Wz}^2$, and $c_0 = (a_1 + u_{Wz})^2 - (\varepsilon_{fr} + \varepsilon_s)^2$. The result clearly shows the linear dispersion for the energy near the Weyl point.

2. Energy spectra in the presence of the complex energy-independent self-energy

In this section, we consider the effects of both the real and imaginary parts in the self-energy. To derive an analytical result, we assume that Γ_0 and Γ_1 are first-order small quantities and $a_1 = 0$. With these approximations, we can derive the energy dispersion close to zero energy up to the first order as

$$\omega \approx -i\Gamma_0v_0 \pm \sqrt{v_1^2\big[d_x^2 + d_y^2 + (d_z - i\gamma_0)^2\big]} \tag{B22}$$

with $v_0 = \varepsilon_s/(\varepsilon_{fr} + \varepsilon_s)$, $v_1 = \varepsilon_{fr}/(\varepsilon_{fr} + \varepsilon_s)$, and $\gamma_0 = \varepsilon_s\Gamma_1/\varepsilon_{fr}$. With nonzero Γ_1, it is easy to see that a Weyl point becomes a Weyl exceptional ring determined by $d_z = 0$ and $d_x^2 + d_y^2 - \gamma_0^2 = 0$.

To analyze the effects of a_1, we assume that it is a first-order small quantity (so is u_{Wz}). We find that a_1 does not affect our results up to the first order. Since a_1 is involved in ε_s, one may think that some higher-order corrections from a_1 are included in ε_s.

3. Renormalization due to the energy-dependent parts in the self-energy

We now study the effects of the energy-dependent parts in the self-energy. The self-energy can be expanded in the Taylor series up to the first order with respect to ω as

$$\Sigma^f \approx a_0 - i\Gamma_0 + (a_1 - i\Gamma_1)\tau_z\sigma_0 + a_{0\omega}\omega + a_{1\omega}\omega\tau_z\sigma_0, \tag{B23}$$

where $a_{0\omega}$ and $a_{1\omega}$ are complex numbers. The inverse of the Green's function is

$$G^{-1} = \omega - \begin{pmatrix} \tilde{\varepsilon}_f + a\tau_z + a_\omega\omega + a_{z\omega}\omega\tau_z & V \\ V & H_c + \varepsilon_s \end{pmatrix} \tag{B24}$$

$$= \begin{pmatrix} \omega(1-a_{0\omega}-a_{1\omega}) - \tilde{\varepsilon}_f - a & 0 & -V & 0 \\ 0 & \omega(1-a_{0\omega}+a_{1\omega}) - \tilde{\varepsilon}_f + a & 0 & -V \\ -V & 0 & & \\ 0 & -V & \omega - H_c - \varepsilon_s & \end{pmatrix}. \tag{B25}$$

We now evaluate the determinant of the inverse of the Green's function,

$$\det(G^{-1}) = \begin{vmatrix} \omega(1-a_{0\omega}-a_{1\omega}) - \tilde{\varepsilon}_f - a & 0 & -V & 0 \\ 0 & \omega(1-a_{0\omega}+a_{1\omega}) - \tilde{\varepsilon}_f + a & 0 & -V \\ -V & 0 & & \\ 0 & -V & \omega - H_c - \varepsilon_s & \end{vmatrix} \tag{B26}$$

$$= \frac{1}{Z_A Z_B} \begin{vmatrix} \omega - Z_A\tilde{\varepsilon}_f - Z_A a & 0 & -\sqrt{Z_A}V & 0 \\ 0 & \omega - Z_B\tilde{\varepsilon}_f + Z_B a & 0 & -\sqrt{Z_B}V \\ -\sqrt{Z_A}V & 0 & & \\ 0 & -\sqrt{Z_B}V & \omega - H_c - \varepsilon_s & \end{vmatrix} \tag{B27}$$

$$= \frac{1}{Z_A Z_B} \begin{vmatrix} \omega - \bar{\varepsilon}_f - \bar{a}\tau_z & -(V_1 + V_2\tau_z) \\ -(V_1 + V_2\tau_z) & \omega - H_c - \varepsilon_s \end{vmatrix} \tag{B28}$$

$$= \frac{1}{Z_A Z_B} |(\omega - \bar{\varepsilon}_f - \bar{a}\tau_z)(\omega - H_c - \varepsilon_s) - (V_1 + V_2\tau_z)^2| \tag{B29}$$

$$= \frac{1}{Z_A Z_B} |(\omega - \bar{\varepsilon}_f - \bar{a}\tau_z)(\omega - H_c - \varepsilon_s) + V_0\tau_z - \bar{V}^2|, \tag{B30}$$

where $Z_A{=}1/(1{-}a_{0\omega} - a_{1\omega})$, $Z_B{=}1/(1{-}a_{0\omega} + a_{1\omega})$, $\bar{\varepsilon}_f = \bar{\varepsilon}_{fr} - i\bar{\Gamma}_0 = [(Z_A + Z_B)\tilde{\varepsilon}_f + (Z_A - Z_B)a]/2$, $\bar{a} = \bar{a}_1 - i\bar{\Gamma}_1 = [(Z_A{-}Z_B)\tilde{\varepsilon}_f + (Z_A + Z_B)a]/2$, $V_1 = (\sqrt{Z_A} + \sqrt{Z_B})V/2$, $V_2 = (\sqrt{Z_A} - \sqrt{Z_B})V/2$, $\bar{V} = \sqrt{V_1^2 + V_2^2}$, and $V_0 = -2V_1V_2$. The determinant can be further reduced to

$$\det(G^{-1}) = \frac{1}{Z_A Z_B} |S^\dagger[(\omega - \bar{\varepsilon}_f - \bar{a}\tau_z)(\omega - H_c - \varepsilon_s) + V_0\tau_z - \bar{V}^2]S| \tag{B31}$$

$$= \frac{1}{Z_A Z_B} |(\omega - \bar{\varepsilon}_f - \bar{a}\tau_z)(\omega - \tilde{H}_c - \varepsilon_s) + V_0\tau_z - \bar{V}^2|, \tag{B32}$$

which is almost the same as Eq. (B6) except a prefactor $1/(Z_A Z_B)$ and a new term $V_0\tau_z$, which can be obtained by replacing $a\varepsilon_s$ with $a\varepsilon_s + V_0$ in Eq. (B6). We now assume that $a_{0\omega}$ and $a_{1\omega}$ are real. Similar to the preceding case, when $\bar{\varepsilon}_f$ and $\bar{a}$ are real, the existence of Weyl points at zero energy requires $\omega = 0$ and

$$\bar{\varepsilon}_f\varepsilon_s - \bar{V}^2 + \bar{a}u_z' = 0, \tag{B33}$$

$$u_x = u_y = 0, \tag{B34}$$

$$\bar{\varepsilon}_f u_z' + \bar{a}\varepsilon_s + V_0 = 0 \tag{B35}$$

which leads to

$$u_z' = u_{Wz} = -\frac{\bar{V}^2\bar{a}_1 + V_0\bar{\varepsilon}_{fr}}{\bar{\varepsilon}_{fr}^2 - \bar{a}_1^2}, \tag{B36}$$

$$\varepsilon_s = \frac{\bar{\varepsilon}_{fr}\bar{V}^2 + V_0\bar{a}_1}{\bar{\varepsilon}_{fr}^2 - \bar{a}_1^2}. \tag{B37}$$

Around the Weyl point, one can also derive the energy dispersion, which is given by Eq. (B21) with renormalized parameters and ε_s and u_{Wz} including extra terms. For clarity, we write down the dispersion explicitly,

$$\omega \approx \frac{2d_z\bar{\varepsilon}_{fr}u_{Wz} \pm \sqrt{\bar{v}_x^2\left(d_x^2 + d_y^2\right) + \bar{v}_z^2 d_z^2}}{\bar{c}_0}, \tag{B38}$$

where $\bar{v}_x^2 = (\bar{a}_1^2 - \bar{\varepsilon}_{fr}^2)\bar{c}_0$, $\bar{v}_z^2 = \bar{v}_x^2 + 4\bar{\varepsilon}_{fr}^2 u_{Wz}^2$, and $\bar{c}_0 = (\bar{a}_1 + u_{Wz})^2 - (\bar{\varepsilon}_{fr} + \varepsilon_s)^2$.

In the presence of the imaginary parts in $\bar{\varepsilon}_f$ and $\bar{a}$, if $\bar{\Gamma}_0$, $\bar{\Gamma}_1$, $\bar{a}_{0\omega}$, and $\bar{a}_{1\omega}$ are first-order small quantities (so is u_{Wz}), the dispersion is also given by Eq. (B22) with renormalized parameters, that is,

$$\omega \approx -i\bar{\Gamma}_0\bar{v}_0 \pm \sqrt{\bar{v}_1^2\left[d_x^2 + d_y^2 + (d_z - i\bar{\gamma}_0)^2\right]} \tag{B39}$$

with $\bar{v}_0 = \varepsilon_s/(\bar{\varepsilon}_{fr}{+}\varepsilon_s)$, $\bar{v}_1{=}\bar{\varepsilon}_{fr}/(\bar{\varepsilon}_{fr}{+}\varepsilon_s)$, and $\bar{\gamma}_0 = \varepsilon_s\bar{\Gamma}_1/\bar{\varepsilon}_{fr}$.

APPENDIX C: THE PERTURBATION THEORY

In this Appendix, we compute the self-energy using the second-order perturbation theory. For the interactions in the form of $U\hat{n}_{i,\uparrow}\hat{n}_{i,\downarrow}$, the f-electron Matsubara Green's function up to the second-order corrections can be described by the one-particle-irreducible diagram, as shown in Fig. 7. The self-energy up to the second-order corrections is expressed as [41,42]

$$\Sigma_{\sigma,j}(i\omega_n) = Un_{-\sigma}^f - U^2T^2\sum_{\omega_x,\omega_y} G_{\sigma,j}^f(i\omega_x)G_{-\sigma,j}^f(i\omega_y) \times G_{-\sigma,j}^f(i\omega_x + i\omega_y - i\omega_n), \tag{C1}$$

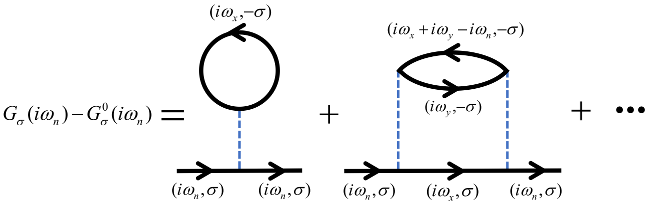

FIG. 7. Diagrammatic expansion for the f-electron Matsubara Green's function.

where $i\omega_n$ is the Matsubara frequency, $\sigma=\uparrow,\downarrow$ is the spin index, $j=A,B$ is the sublattice index, T is the temperature, and $G^f_{\sigma,j}(i\omega_n)$ is the corresponding f-electron Matsubara Green's function. With time-reversal symmetry, Matsubara Green's functions of spin up and down have the same form and we thus drop the spin index. The blue dashed line in Fig. 7 represents the interaction term connecting four Matsubara Green's functions of f electrons. For any order of perturbation, one can show with the method of the equation of motion [42,43], the self-energy must connect with Matsubara Green's functions of f electrons from the same sublattices. It indicates, for the matrix form of self-energy, only diagonal terms of f electrons are nonzero.

The first-order self-energy term can be understood as the Hartree part of the electron's self-energy and is not a function of the frequency and thus can be contained in ε_f. By performing the sum over the Matsubara frequency, the second-order self-energy can be reduced to [41,42]

$$\begin{aligned}\Sigma_j(\omega)\\ &= -U^2\iiint_{-\infty}^{+\infty} d\omega_1 d\omega_2 d\omega_3 \rho^f_j(\omega_1)\rho^f_j(\omega_2)\rho^f_j(\omega_3)\\ &\quad\times\frac{n_F(\omega_1)n_F(\omega_2)n_F(-\omega_3)+n_F(-\omega_1)n_F(-\omega_2)n_F(\omega_3)}{\omega-\omega_1-\omega_2+\omega_3+i0^+},\end{aligned} \tag{C2}$$

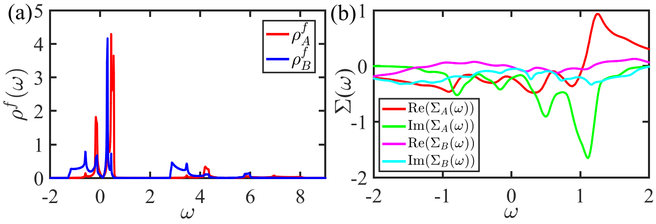

FIG. 8. (a) The density of states for the f electrons at sublattices A and B without interactions as a function of the energy ω. (b) The numerically computed self-energy based on Eq. (C2) at the temperature $T=1/6$. Here, $t=0.5$, $m=1.2$, $\lambda=0.6$, $V=2$, $U=2$, $\varepsilon_f=1.125$, and $\varepsilon_s=4$.

where $n_F=1/(e^{\omega/T}+1)$ is the Fermi-Dirac distribution function, and $\rho^f_j(\omega)=-\frac{1}{\pi}\mathrm{Im}G^f_j(\omega+i0^+)$ is f-electron density of states at the sublattice j in the absence of interactions.

Figure 8(a) shows the density of states of the f electron $\rho^f_{A/B}(\omega)$ with $t=0.5$, $m=1.2$, $\lambda=0.6$, $V=2$, $U=2$, $\varepsilon_f=1.125$, and $\varepsilon_s=-4$, which is used to compute the self-energy. The densities of states vanish at the energy close to the zero energy, indicating the existence of Weyl points there. Figure 8(b) displays the numerically calculated second-order self-energy based on Eq. (C2) at the temperature $T=1/6$. One can observe that the self-energy exhibits oscillations, which result from the Van Hove singularities in the density of states. In addition, the amplitude of the self-energy at the sublattice A is much larger than that at the sublattice B due to the more compact $\rho^f_A(\omega)$.

We calculate the self-energies at different temperatures and perform the Taylor expansion with respect to ω near the zero energy,

$$\Sigma^f(\omega)\approx a_0-i\Gamma_0+(a_1-i\Gamma_1)\tau_z+a_{0\omega}\omega+a_{1\omega}\omega\tau_z \tag{C3}$$

$$=\begin{pmatrix} a_{0A}+a_{1A}\omega & 0\\ 0 & a_{0B}+a_{1B}\omega\end{pmatrix}, \tag{C4}$$

where $\mathrm{Re}(a_{0A})=a_0+a_1$, $\mathrm{Im}(a_{0A})=-(\Gamma_0+\Gamma_1)$, $\mathrm{Re}(a_{1A})=a_{0\omega}+a_{1\omega}$, $\mathrm{Re}(a_{0B})=a_0-a_1$, $\mathrm{Im}(a_{0B})=-(\Gamma_0-\Gamma_1)$, and

TABLE I. List of Taylor coefficients for the self-energy at different temperatures evaluated by Eq. (C2). Here $t=0.5$, $m=1.2$, $\lambda=0.6$, $V=2$, $U=2$, $\varepsilon_f=1.125$, and $\varepsilon_s=4$.

T	$\mathrm{Re}(a_{0A})$	$\mathrm{Re}(a_{1A})$	$\mathrm{Im}(a_{0A})$	$\mathrm{Re}(a_{0B})$	$\mathrm{Re}(a_{1B})$	$\mathrm{Im}(a_{0B})$	Γ_1
1/30	−0.1921	−0.5401	−0.0012	−0.0350	−0.2381	-1.76×10^{-4}	5.32×10^{-4}
1/28	−0.1932	−0.5423	−0.0016	−0.0353	−0.2391	-2.44×10^{-4}	6.63×10^{-4}
1/26	−0.1944	−0.5451	−0.0020	−0.0357	−0.2404	-3.48×10^{-4}	8.19×10^{-4}
1/24	−0.1960	−0.5486	−0.0025	−0.0362	−0.2422	-5.11×10^{-4}	0.0010
1/22	−0.1980	−0.5530	−0.0033	−0.0367	−0.2447	-7.65×10^{-4}	0.0013
1/20	−0.2004	−0.5588	−0.0045	−0.0372	−0.2484	−0.0012	0.0016
1/18	−0.2033	−0.5662	−0.0062	−0.0377	−0.2537	−0.0018	0.0022
1/16	−0.2067	−0.5753	−0.0092	−0.0379	−0.2615	−0.0030	0.0031
1/14	−0.2107	−0.5860	−0.0147	−0.0377	−0.2731	−0.0049	0.0049
1/12	−0.2149	−0.5963	−0.0252	−0.0364	−0.2899	−0.0084	0.0084
1/10	−0.2190	−0.6009	−0.0457	−0.0333	−0.3137	−0.0148	0.0155
1/8	−0.2222	−0.5881	−0.0864	−0.0274	−0.3443	−0.0266	0.0299
1/6	−0.2229	−0.5415	−0.1640	−0.0179	−0.3756	−0.0496	0.0572

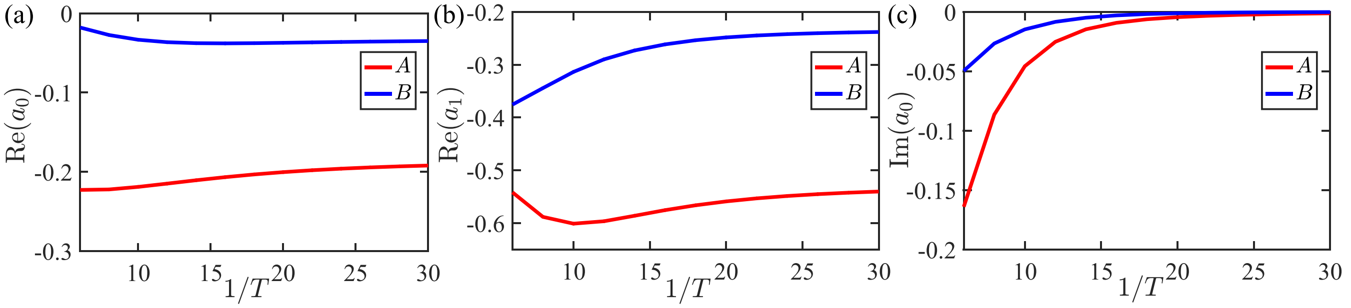

FIG. 9. Plots of Taylor coefficients for the self-energy at different temperatures using the data listed in Table I. Here, $t = 0.5$, $m = 1.2$, $\lambda = 0.6$, $V = 2$, $U = 2$, $\varepsilon_f = 1.125$, and $\varepsilon_s = 4$.

$\text{Re}(a_{1B}) = a_{0\omega} - a_{1\omega}$. The numerically computed Taylor coefficients are listed in Table I, where $\text{Im}(a_{1A})$ and $\text{Im}(a_{1B})$ are not displayed as their values are much smaller than those of the corresponding real parts. To clearly see their change with respect to temperatures, we also provide the curve description in Fig. 9. As discussed in the preceding section, the existence of $\text{Re}(a_{0A})$ and $\text{Re}(a_{0B})$ changes the position of Weyl points in momentum space and their energy (if ε_s is held fixed). Figure 9(a) tells us that $\text{Re}(a_{0A})$ and $\text{Re}(a_{0B})$ only slightly change with temperatures, indicating that the position and energy of Weyl points change slightly. $\text{Im}(a_{0A})$ [$\text{Im}(a_{0B})$] reveal the inverse of the lifetime of quasiparticles at sublattice A (B) and must be negative. Both $|\text{Im}(a_{0A})|$ and $|\text{Im}(a_{0B})|$ increase with the rise of temperatures, and their difference Γ_1 also increases significantly with temperatures, leading to enlarged Weyl exceptional rings as temperatures rise, which further merge into two exceptional rings as discussed in the main text. As discussed in the preceding section, $\text{Re}(a_{1A})$ and $\text{Re}(a_{1B})$ renormalize system parameters and thus do not affect the qualitative feature of the energy spectrum.

APPENDIX D: THE SPECTRAL FUNCTIONS WITH RESPECT TO THE ENERGY

In the main text, we have shown the spectral functions with respect to the energy at three fixed points in momentum space. Here, we analyze the features of the spectral functions as functions of both ω and $\boldsymbol{k}$. We consider two cases: One is along the k_x line with $k_y = 0$ and $k_z = 2\pi$ which crosses the Fermi tube, and the other is along the k_z line with $k_x = -0.675$ and $k_y = 0$

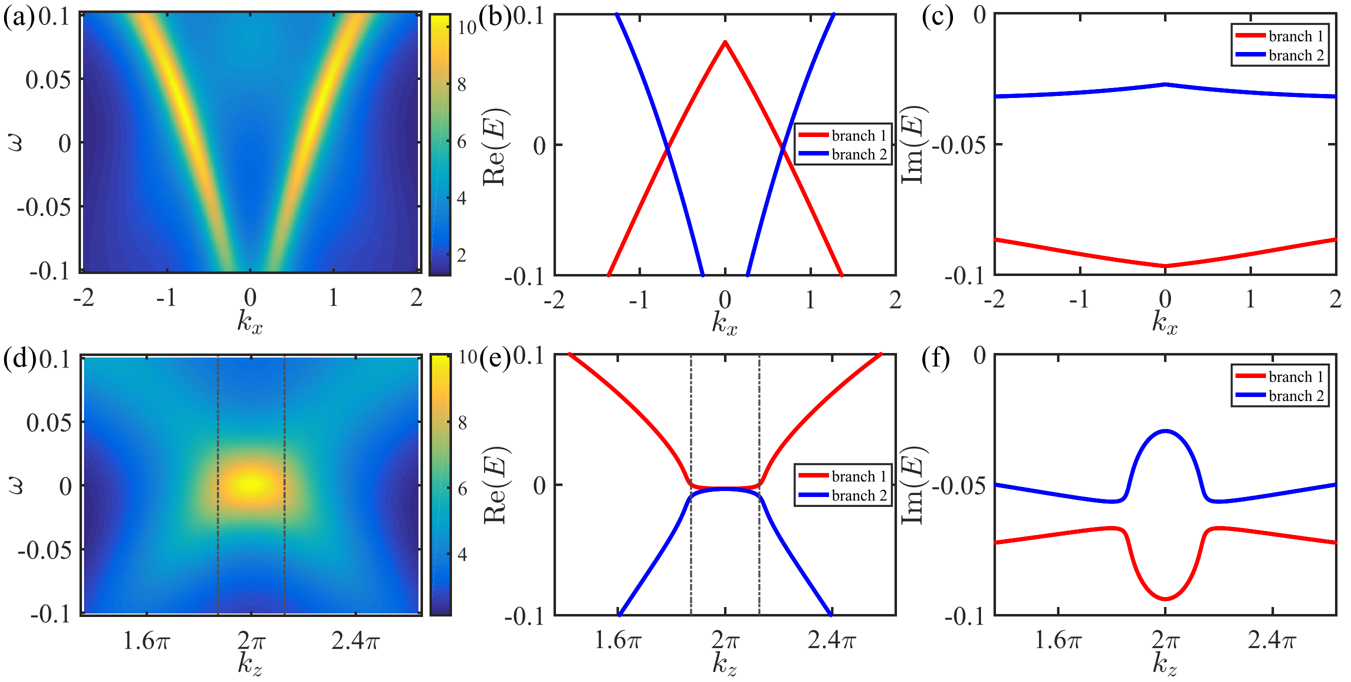

FIG. 10. (a) The spectral function $\rho(\omega, \boldsymbol{k})$ with respect to ω and k_x with $k_y = 0$ and $k_z = 2\pi$. The real and imaginary parts of the corresponding energy spectrum for the second and third bands of the effective Hamiltonian are plotted in (b) and (c), respectively. (d) The spectral function $\rho(\omega, \boldsymbol{k})$ with respect to ω and k_z with $k_x = -0.675$ and $k_y = 0$ with the real and imaginary parts of the corresponding energy spectrum plotted in (e) and (f), respectively. In (d) and (e), two vertical lines refer to the positions where the real part of the energy spectrum begins to split. Here, $t = 0.5$, $m = 1.2$, $\lambda = 0.6$, $V = 2$, $U = 2$, $\varepsilon_f = 1.125$, $\varepsilon_s = 4$, and $T = 1/6$.

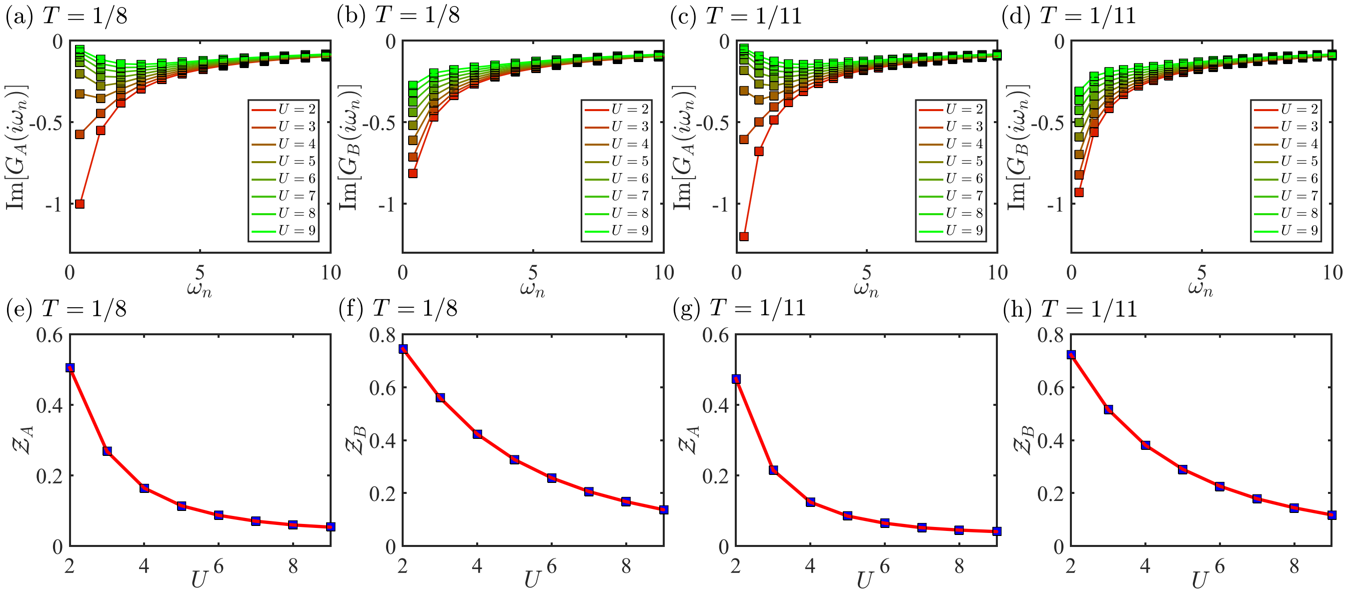

FIG. 11. (a)–(d) Imaginary parts of the Matsubara Green's function and (e)–(h) quasiparticle weights for f electrons on sublattice A or B with respect to the interaction U at $T = 1/8$ or $T = 1/11$.

which is along the Fermi tube. In Fig. 10, we plot the spectral functions at the temperature $T = 1/6$, which are numerically calculated by the second-order perturbation theory. In the former case [see Fig. 10(a)], there appear two bright lines crossing zero energy corresponding to two exceptional points, which agree well with the blue branch in the energy spectrum (the poles of the Green's function) shown in Fig. 10(b). One may wonder why the other red branch disappears in the spectral function. To interpret the phenomenon, we plot the imaginary parts of the energy spectrum in Fig. 10(c), illustrating that the red branch has larger absolute values of the imaginary parts. With larger imaginary values, the spectral functions are broader so that this branch is invisible compared to the blue one with smaller imaginary values. In the latter case, the spectral function exhibits a bright region around $\omega = 0$ which extends along k_z near $k_z = 2\pi$, corresponding to the zero-energy part in the energy dispersion [see Fig. 10(e)]. The energy spectrum then splits into two branches as k_z deviates from the flat region, which can also be observed in the spectral function. For the splitting parts, the peak becomes wider and weaker since the corresponding imaginary parts of the energy spectra are larger [see Fig. 10(f)]. Note that while the positions in the spectral function where the splitting happens are slightly different from those in the energy spectrum, they are closely related. Also note that the imaginary parts of the two branches do not touch because the chosen momenta do not cross exceptional rings due to the fact that the Fermi surface slightly deviates from a cylinder shape and takes the shape of a barrel.

APPENDIX E: OTHER DATA ANALYSIS ABOUT THE DMFT CALCULATION

To confirm the reliability of our DMFT calculations, we use the existing scripts to compute the Mott transition with the increase of the interaction strength U at different temperatures. The phase transition can be identified by the imaginary parts of the Matsubara Green's function $G(i\omega_n)$ and the quasiparticle weights $\mathcal{Z}$. A significant decline in the $|\mathrm{Im}G(i\omega_n)|$ near $\omega_0 \equiv \pi T$ is observed in Figs. 11(a)–11(d), which is one of the characteristics when the Mott transition happens. We point out that there is a site-selective Mott-insulating behavior between A and B sites [44]. While electrons on sublattice A enter into the Mott-insulating phase (e.g., $U > 4$), electrons on sublattice B are still in the metallic phase. The distinct behavior arises from the breaking of inversion symmetry, which is also crucial for the emergence of different quasiparticle lifetimes on different sublattices. The Mott transition can also be identified by quasiparticle weights $\mathcal{Z}$, which can be calculated approximately at low temperatures by

$$\mathcal{Z} \cong \left[1 - \frac{\mathrm{Im}\Sigma(i\omega_0)}{\omega_0}\right]^{-1}. \tag{E1}$$

The results of $\mathcal{Z}$ are shown in Figs. 11(e)–11(h). We see that with the increase of U, $\mathcal{Z}$ on sublattice A decreases toward zero, signaling a transition from a metallic phase to the Mott-insulating phase. Compared with the quasiparticle weights on sublattice A, the decline of the weights on sublattice B with the interaction is slower and smoother, which agrees well with the result of the Matsubara Green's function.

---

[1] M. Imada, A. Fujimori, and Y. Tokura, Rev. Mod. Phys. **70**, 1039 (1998).

[2] E. Demler, W. Hanke, and S.-C. Zhang, Rev. Mod. Phys. **76**, 909 (2004).

[3] P. A. Lee, N. Nagaosa, and X.-G. Wen, Rev. Mod. Phys. **78**, 17 (2006).

[4] M. Capone, M. Fabrizio, C. Castellani, and E. Tosatti, Rev. Mod. Phys. **81**, 943 (2009).

[5] S. Paschen and Q. Si, Nat. Rev. Phys. **3**, 9 (2021).

[6] B. Keimer, S. A. Kivelson, M. R. Norman, S. Uchida, and J. Zaanen, Nature (London) **518**, 179 (2015).

[7] Y. Xu, F. Zhang, and C. Zhang, Phys. Rev. Lett. **115**, 265304 (2015).

[8] A. A. Soluyanov, D. Gresch, Z. Wang, Q.-S. Wu, M. Troyer, X. Dai, and B. A. Bernevig, Nature (London) **527**, 495 (2015).

[9] Y. Nagai, Y. Qi, H. Isobe, V. Kozii, and L. Fu, Phys. Rev. Lett. **125**, 227204 (2020).

[10] T. Yoshida, R. Peters, and N. Kawakami, Phys. Rev. B **98**, 035141 (2018).

[11] T. Yoshida, R. Peters, N. Kawakami, and Y. Hatsugai, Phys. Rev. B **99**, 121101(R) (2019).

[12] K. Kimura, T. Yoshida, and N. Kawakami, Phys. Rev. B **100**, 115124 (2019).

[13] Y. Michishita, T. Yoshida, and R. Peters, Phys. Rev. B **101**, 085122 (2020).

[14] Y. Michishita and R. Peters, Phys. Rev. Lett. **124**, 196401 (2020).

[15] Y. Xu, S.-T. Wang, and L.-M. Duan, Phys. Rev. Lett. **118**, 045701 (2017).

[16] A. Cerjan, S. Huang, M. Wang, K. P. Chen, Y. Chong, and M. C. Rechtsman, Nat. Photon. **13**, 623 (2019).

[17] A. A. Zyuzin and A. Y. Zyuzin, Phys. Rev. B **97**, 041203(R) (2018).

[18] A. Cerjan, M. Xiao, L. Yuan, and S. Fan, Phys. Rev. B **97**, 075128 (2018).

[19] J. Carlström and E. J. Bergholtz, Phys. Rev. A **98**, 042114 (2018).

[20] Z. Yang and J. Hu, Phys. Rev. B **99**, 081102(R) (2019).

[21] H.-Q. Wang, J.-W. Ruan, and H.-J. Zhang, Phys. Rev. B **99**, 075130 (2019).

[22] K. Kawabata, T. Bessho, and M. Sato, Phys. Rev. Lett. **123**, 066405 (2019).

[23] T. Liu, J. J. He, Z. Yang, and F. Nori, Phys. Rev. Lett. **127**, 196801 (2021).

[24] M. Dzero, K. Sun, V. Galitski, and P. Coleman, Phys. Rev. Lett. **104**, 106408 (2010).

[25] M. Dzero, K. Sun, P. Coleman, and V. Galitski, Phys. Rev. B **85**, 045130 (2012).

[26] F. Lu, J. Z. Zhao, H. Weng, Z. Fang, and X. Dai, Phys. Rev. Lett. **110**, 096401 (2013).

[27] Y. Xu, C. Yue, H. Weng, and X. Dai, Phys. Rev. X **7**, 011027 (2017).

[28] H.-H. Lai, S. E. Grefe, S. Paschen, and Q. Si, Proc. Natl. Acad. Sci. USA **115**, 93 (2018).

[29] S. E. Grefe, H.-H. Lai, S. Paschen, and Q. Si, Phys. Rev. B **101**, 075138 (2020).

[30] S. Dzsaber, L. Prochaska, A. Sidorenko, G. Eguchi, R. Svagera, M. Waas, A. Prokofiev, Q. Si, and S. Paschen, Phys. Rev. Lett. **118**, 246601 (2017).

[31] S. Dzsaber, X. Yan, M. Taupin, G. Eguchi, A. Prokofiev, T. Shiroka, P. Blaha, O. Rubel, S. E. Grefe, H.-H. Lai, Q. Si, and S. Paschen, Proc. Natl. Acad. Sci. USA **118**, e2013386118 (2021).

[32] E. M. Brüning, M. Brando, M. Baenitz, A. Bentien, A. M. Strydom, R. E. Walstedt, and F. Steglich, Phys. Rev. B **82**, 125115 (2010).

[33] V. Guritanu *et al.*, Phys. Rev. B **87**, 115129 (2013).

[34] M. Sundermann *et al.*, Sci. Rep. **5**, 17937 (2015).

[35] P. Wissgott and K. Held, Eur. Phys. J. B **89**, 5 (2016).

[36] L. Fu, C. L. Kane, and E. J. Mele, Phys. Rev. Lett. **98**, 106803 (2007).

[37] H. Shen, B. Zhen, and L. Fu, Phys. Rev. Lett. **120**, 146402 (2018).

[38] Z. Gong, Y. Ashida, K. Kawabata, K. Takasan, S. Higashikawa, and M. Ueda, Phys. Rev. X **8**, 031079 (2018).

[39] Q.-B. Zeng and Y. Xu, Phys. Rev. Res. **2**, 033052 (2020).

[40] O. Parcollet, M. Ferrero, T. Ayral, H. Hafermann, I. Krivenko, L. Messio, and P. Seth, Comput. Phys. Commun. **196**, 398 (2015).

[41] H. Schweitzer and G. Czycholl, Solid State Commun. **69**, 171 (1989).

[42] H. Schweitzer and G. Czycholl, Phys. B: Condens. Matter **163**, 415 (1990).

[43] G. Górski and J. Mizia, Phys. B: Condens. Matter **427**, 42 (2013).

[44] H. Park, A. J. Millis, and C. A. Marianetti, Phys. Rev. Lett. **109**, 156402 (2012).